SURFACE CHEMISTRY

Unraveling CO adsorption on model single-atom catalysts

Jan Hulva[1]*, Matthias Meier[1,2]*, Roland Bliem[1]†, Zdenek Jakub[1], Florian Kraushofer[1], Michael Schmid[1], Ulrike Diebold[1], Cesare Franchini[2,3], Gareth S. Parkinson[1]‡

Understanding how the local environment of a "single-atom" catalyst affects stability and reactivity remains a challenge. We present an in-depth study of copper$_1$, silver$_1$, gold$_1$, nickel$_1$, palladium$_1$, platinum$_1$, rhodium$_1$, and iridium$_1$ species on Fe_3O_4(001), a model support in which all metals occupy the same twofold-coordinated adsorption site upon deposition at room temperature. Surface science techniques revealed that CO adsorption strength at single metal sites differs from the respective metal surfaces and supported clusters. Charge transfer into the support modifies the d-states of the metal atom and the strength of the metal–CO bond. These effects could strengthen the bond (as for Ag_1–CO) or weaken it (as for Ni_1–CO), but CO-induced structural distortions reduce adsorption energies from those expected on the basis of electronic structure alone. The extent of the relaxations depends on the local geometry and could be predicted by analogy to coordination chemistry.

The reactivity of oxide-supported metal nanoparticle catalysts is traditionally understood by using the d-band model, which was developed for extended metal surfaces (*1*). Such a picture cannot be applied to so-called "single-atom" catalysts (*2*–*8*) because the isolated metal atoms are stabilized by chemical bonds to the support and are often charged. In this regard, single-atom catalysis systems resemble coordination complexes, and there is much excitement at the prospect that single-atom catalysts can be used to "heterogenize" problematic reactions currently performed in solution (*9*–*11*). Although there are similarities, there are also practical differences. Homogeneous catalysts are designed for purpose on the basis of a fundamental understanding of the structure-function relationship, and the ligands play an important role in activating reactants and stabilizing intermediates. Complexes containing O^{2-} ligands are rare (*5*), and the binding environment of the metal adatom on the metal oxide is difficult to ascertain and control. Because robust, inexpensive metal oxides are set to continue as the support of choice in single-atom catalysis, it is vital to learn how the coordination of the metal site on an oxide surface affects its adsorption properties and ultimately catalytic activity.

Most studies of oxide-supported single-atom catalysts feature transmission electron microscopy images (*12*) of powder samples showing that the metal adatoms align with the cationic sublattice. These structures are in agreement with x-ray absorption near-edge structure spectra, which typically suggest coordination to oxygen. Density functional theory (DFT) calculations (*13*–*16*) also predict such sites to be most stable (albeit on simplified models of the support surface). Often, a positive charge state can be inferred from x-ray photoelectron spectroscopy, infrared vibrational spectroscopy, or both of adsorbed CO (*8*, *13*). More definitive interpretation requires simulated or experimental reference spectra and, thus, a knowledge of the atomic configuration around the active site (*17*). Nevertheless, the charge state of the metal is frequently invoked to explain reactivity, although this explanation is not without controversy. The cationic nature of Pt_1 has been linked to both stronger (*8*) and weaker (*15*) CO adsorption, with diametrically opposed conclusions regarding CO oxidation activity.

In this paper, we combine temperature-programmed desorption, x-ray photoelectron spectroscopy, scanning tunneling microscopy, and DFT calculations to study CO adsorption on a series of model single-atom catalysts: Cu_1, Ag_1, Au_1, Ni_1, Pd_1, Pt_1, Rh_1, and Ir_1 atoms on Fe_3O_4(001). Upon deposition at room temperature, all of the metals assume the same twofold coordination to surface oxygen, which allows for direct comparison. We selected CO as the probe molecule because of the abundance of experimental and computational results on metal surfaces and nanoparticles and because many single-atom catalysis studies focus on CO oxidation and the water gas shift reaction, in which CO is a reactant. Moreover, the stretching frequency of adsorbed CO is often used to probe the charge state of the metal in single-atom catalysis systems (*8*, *13*, *17*, *18*), which makes a detailed understanding of the metal-CO interaction particularly important.

Our results show that the CO binding strength broadly follows the trends established for the corresponding low-index metal surfaces, i.e., group 9 > 10 > 11, but differences emerge within the groups. Our DFT-based calculations reproduce the experimental data well and show that the adsorption energy is linked to both the electronic structure of the adatom and adsorbate-induced structural relaxations of the system. The combination of the two effects differs from metal to metal because each responds differently to the twofold-coordination environment and because each has a different relative affinity for CO and O. Where the agreement between experiment and theory is imperfect, we show that the catalyst structure evolves during the experiment. Ultimately, our results corroborate that the behavior of single-atom catalysts is better rationalized by analogy to coordination complexes than to metal nanoparticles and that the reactivity of the metal atoms in single-atom catalysis can be tuned if the coordination environment can be controlled.

The experiments described here were performed on several natural Fe_3O_4(001) single crystals over a period of 4 years. The samples were prepared in ultrahigh vacuum by cycles of Ar^+ or Ne^+ sputtering and 900-K annealing. The resulting surfaces exhibited the $(\sqrt{2} \times \sqrt{2})$R45° low-energy electron diffraction pattern and scanning tunneling microscopy signature characteristic of the so-called subsurface cation vacancy reconstruction (*19*, *20*), which is known to stabilize dense arrays of metal atoms to temperatures as high as 700 K (*20*, *21*). Metal was evaporated directly onto the as-prepared Fe_3O_4(001) support in ultrahigh vacuum (i.e., no additional ligands are present). We define coverages in monolayers [ML, which corresponds to 1 atom per $(\sqrt{2} \times \sqrt{2})$R45° unit cell, or 1.42×10^{14} per square centimeter]. In Fig. 1A, scanning tunneling microscopy shows that Cu, Ag, Au, Ni, Pd, Pt, Rh, and Ir atoms all adsorb at the same location between the underlying rows of surface Fe atoms. The surface oxygen atoms are not imaged in scanning tunneling microscopy because they have no electronic states in the vicinity of the Fermi level, but their position is well known from quantitative electron (*19*) and x-ray diffraction (*22*) measurements and DFT-based calculations. The as-deposited structure and thermal stability of the adatom systems shown in Fig. 1A have all been thoroughly characterized previously (*21*, *23*–*30*), which makes this an ideal model system to systematically compare the adatom properties. The adsorption site is twofold coordinated to the surface oxygen atoms that do not have a subsurface tetrahedral Fe neighbor (Cu is shown as an example in Fig. 1B). This is a site where the next Fe cation would reside if the bulk structure continued outward, and the nearest neighbor distance of these sites is the periodicity of the surface reconstruction (8.4 Å). The height of the adatoms above the surface (z) varies

[1]Institute of Applied Physics, TU Wien, Vienna, Austria. [2]Computational Materials Physics, University of Vienna, Vienna, Austria. [3]Alma Mater Studiorum–Università di Bologna, Bologna, Italy.
*These authors contributed equally to this work. †Present address: Advanced Research Center for Nanolithography, Science Park 106, 1098XG Amsterdam, Netherlands.
‡Corresponding author. Email: parkinson@iap.tuwien.ac.at

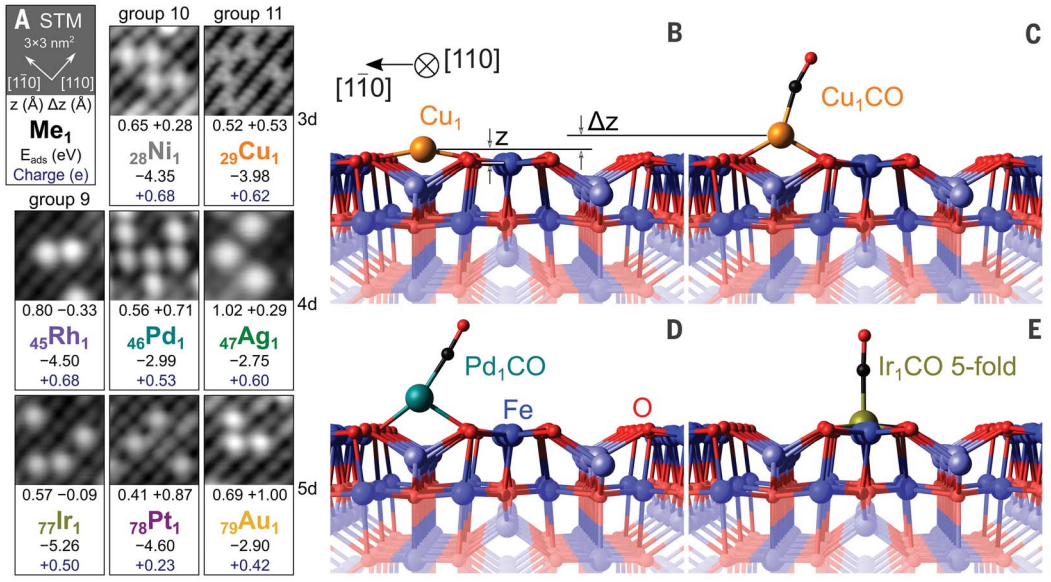

Fig. 1. Characterization of the Fe_3O_4(001)-based single-atom catalysis model systems. (**A**) Representative scanning tunneling microscopy images (V_{sample} = +1 to 1.5 V, I_{tunnel} = 0.1 to 0.3 nA) showing metal adatoms adsorbed midway between the bright Fe rows of the Fe_3O_4(001) support. This corresponds to the twofold adsorption geometry. The nearest neighbor distance is the periodicity of the surface reconstruction (8.4 Å). Alongside each image are the computationally-derived adsorption energies, Bader charges, and heights of the Me_1 adatom (z) above the surface Fe atoms in the twofold adsorption geometry, as well as the CO-induced vertical displacement (Δz). (**B** to **D**) Computationally-derived minimum-energy structure for the twofold-coordinated Cu_1/Fe_3O_4(001) adatom before (B) and after (C) adsorption of CO, as well as the Pd_1CO carbonyl (D). Both are lifted from the surface upon CO adsorption. (**E**) IrCO replaces a fivefold-coordinated surface Fe atom during the temperature-programmed desorption ramp, meaning that CO desorption ultimately occurs from the depicted fivefold Ir_1 geometry (*29*).

greatly, and we recently measured this parameter for Cu, Ag, and Ni (*27*, *28*).

These data were used to benchmark our theoretical approach, and Fig. 1A shows results from calculations using the optimal density functional theory (DFT+U) parameters [effective Hubbard U parameter (U_{eff}) = 3.61 eV, optB88-DF functional] (*27*, *28*). All of the metal adatoms are cationic with Bader charges in the range 0.23*e* to 0.68*e*. Although the Bader-derived charges generally underestimate the formal oxidation states, they are a useful scheme to correlate effective and ionic charges (*17*, *31*). For example, the Ni adatom exhibited a Bader charge (+0.68*e*) midway between the metal (+0.01*e*) and a fivefold-coordinated cation at the NiO(100) surface (+1.19*e*). Because the cations in NiO are nominally 2+, we assign a 1+ oxidation state for the Ni_1/Fe_3O_4(001) adatom. The charge transferred from the metal atom is donated to the undercoordinated surface oxygen atoms, which have a small magnetic moment on the clean surface (*19*). These revert to zero magnetic moment and an O^{2-} state when their fourfold environment is recovered. Ag, Au, and Pd are rather weakly bound (E_{ads} = −2.75, −2.90, and −2.99 eV, respectively), whereas Ir shows the strongest interaction (E_{ads} = −5.26 eV). Cu, Ni, Rh, and Pt lie in between −3.98 and −4.60 eV. Thus, the binding energy scales somewhat with the oxophilicity of the metal, which is in line with previous reports for oxide-supported metal clusters (*32*) and single-atom catalysts (*33*). Ni (*25*), Rh (*30*), and Ir (*29*) adatoms were ultimately unstable against incorporation into the surface lattice, which is important in interpreting our results.

To determine how strongly CO binds to the different metal adatoms, we conducted a series of temperature-programmed desorption experiments. The interaction of CO with the Fe_3O_4(001) support is weak (*34*), and the molecule desorbs from surface Fe^{3+} sites in two peaks between 60 and 100 K (fig. S1). Additional small desorption peaks between 100 and 220 K arise from CO desorbing from Fe^{2+}-containing defects in the surface, such as antiphase domain boundaries and step edges (*34*). The gray curves in Figs. 2, A to G, show the "clean-surface" CO temperature–programmed desorption data acquired before adsorption of the metal adatoms (omitting the much larger desorption peaks from the regular Fe sites, fig. S1). The small differences in the relative intensity of the different defect peaks from experiment to experiment were the result of these data being acquired with several different Fe_3O_4(001) samples.

The colored curves in Fig. 2 show selected CO temperature–programmed desorption data obtained after deposition of metal adatoms at 300 K. In each case, the sample was cooled to 100 K, CO was adsorbed, and the sample was heated with a ramp of 1 K s^{-1}. An arrow marks the temperature-programmed desorption peak corresponding to desorption of CO from the metal adatom in each case. The peak assignments were the result of a series of scanning tunneling microscopy, x-ray photoelectron spectroscopy, and temperature-programmed desorption experiments for different adatom coverages and experimental conditions. This assignment was necessary because the Me_1/Fe_3O_4(001) systems were not static and evolved differently upon CO exposure and heating. We briefly summarize the basis of the assignment for each metal. Further details can be found in the supplementary materials, and an exhaustive account of these experiments is contained within the Ph.D. thesis by Hulva (*35*).

Ag and Cu were straightforward to interpret because scanning tunneling microscopy measurements showed that the adatom phase was stable for densities up to almost 0.5 ML (*27*). Moreover, the adatom arrays were thermally stable to temperatures as high as 700 K (*24*) as well as after exposure to CO. For all adatoms studied in this work, CO adsorption induced a positive core-level shift in the photoemission spectra associated with the adatom (fig. S2) that disappeared when CO desorbed from the adatom, along with the peak in carbon 1s from the adsorbed CO (fig. S3).

For both Cu and Ag, a small shoulder was present on the high-temperature side of the main temperature-programmed desorption peak. This shoulder resulted from a fraction of adatoms occupying a metastable geometry after room-temperature deposition and decreased in intensity after annealing the system before CO adsorption (figs. S4 and S5). For Cu, an additional sharp peak was observed at 120 K that could arise from $Cu(CO)_2$ dicarbonyls, which can be stabilized at low temperature. Details regarding dicarbonyl formation, including how the structures mimic common coordination complexes, can be found in the supplementary materials (tables S3 and S4).

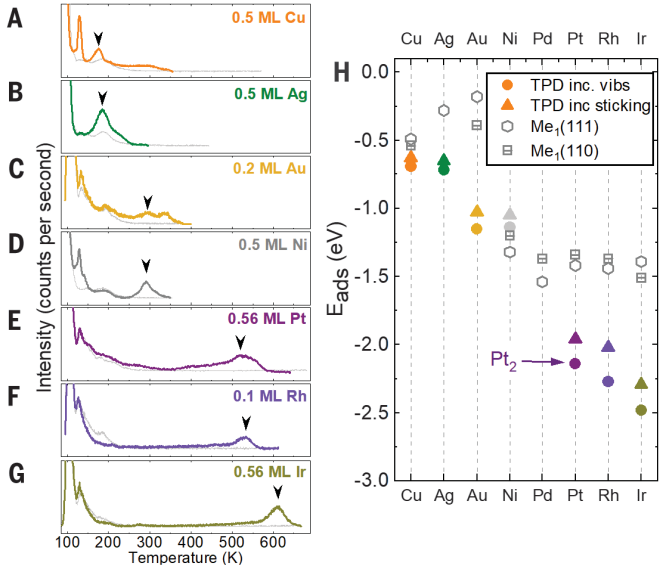

Fig. 2. Determining the CO adsorption on $Me_1/Fe_3O_4(001)$ model catalysts with temperature-programmed desorption. (**A** to **G**) CO temperature–programmed desorption (TPD) curves for various adatoms (1 ML corresponds to 1 metal atom per surface unit cell, or 1.42×10^{14} atoms per square centimeter). Desorption peaks associated with the metal adatoms are labeled using an arrow. Reasoning behind their position is given in the main text. The light-gray curves show CO temperature–programmed desorption data acquired for the ultrahigh vacuum–prepared $Fe_3O_4(001)$ surface before deposition of the metal. (**H**) Plot of experimental and calculated CO adsorption and desorption energies (E_d), alongside experimental values for respective metal (111) and (110) surfaces taken from the literature (table S6).

Au was the most complicated system studied in this work because clusters coexisted with adatoms even at very low coverages [<0.15 ML (*21*)] and because two CO temperature–programmed desorption peaks grew together at 335 K and 285 to 300 K as the Au coverage was increased (fig. S6). These results suggest the presence of two inequivalent sites for adsorption. We assigned the peak at 285 to 300 K to CO desorbing from regular Au adatoms because pre-annealing the system before CO adsorption increased the intensity of the 300-K peak relative to the 335-K peak and because the 335-K peak intensity increased after exposure to water (fig. S7). The latter observation suggested that the 335-K peak was probably related to Au adatoms interacting with surface hydroxyl groups, as has been observed previously by scanning tunneling microscopy for Pd adatoms on this surface (*23*).

Turning to the group 10 metals, the CO peak desorbing from Ni_1 at 300 K was straightforward to assign on the basis of the CO-induced core-level shift. The additional peak at 200 K may be related to Ni incorporated in the surface, as Ni can move to subsurface sites at room temperature (*28*). Temperature-programmed desorption data for Pd are not shown because CO adsorption destabilized the adatoms and led to rapid agglomeration (*23*). A similar process occurred for Pt, but the temperature-programmed desorption data show a main peak that resulted from the decomposition of $Pt_2(CO)_2$ species (*26*).

The CO desorption peaks from the group 9 Rh and Ir adatoms are again straightforward to assign, although these metals incorporated into the oxide lattice when CO desorbed (*29*). Thus, the postdesorption x-ray photoelectron spectroscopy peaks of Rh and Ir exhibited a higher binding energy than the initial twofold adatom (*29*) rather than shifting back to the as-deposited position. The data acquired at 0.1-ML Rh coverage are shown because this metal exhibited a lower-temperature desorption peak for coverages above 0.2 ML (*35*).

In Fig. 2H, we convert the temperature-programmed desorption peak temperatures into desorption energies and plot these alongside values for the corresponding (111) and (110) metal surfaces obtained from table S6 and ref (*36*). Assuming the adsorption-desorption process is reversible and there is no barrier for adsorption, the desorption energy is equivalent to E_{ads}. The basic trend is somewhat similar to the adatoms studied in this work (i.e., group 9 > 10 > 11), but there are large differences in the absolute magnitudes as well as in the tendencies within groups. Most studies on extended metal surfaces typically use the Redhead (*37*) or Polanyi-Wigner equation with a preexponential factor of ~10^{13} s^{-1}, which corresponds to a molecule adsorbed in a corrugation-free surface potential. In our case, however, scanning tunneling microscopy experiments before and after CO desorption reveal no cluster formation, which suggests the CO molecule is constrained at an immobile adatom even at the desorption temperature. We thus treat the system as an ideal two-dimensional lattice gas (*38*). The low density of adsorption sites results in much higher preexponential factors, and assuming the adsorbed CO has three vibrational modes with a frequency of 400 cm^{-1}, we obtain values between 1.27×10^{19} s^{-1} for Cu and 3.25×10^{19} s^{-1} for Ir. The upper and lower bounds for the experimental energies include a temperature uncertainty of ±10 K (±20 K for Au).

Figure 2H also includes the adsorption energies determined from DFT+U for a single CO molecule adsorbed on the metal adatoms (Fig. 2H, solid circles, and table S3). The calculations track the experimental trend with an offset of approximately −0.2 eV for all metals (other than Pt, which formed dimers), which shows that the optB88-DF functional systematically overbinds the CO molecule (as suggested previously for water adsorption on Fe_3O_4) (*39*). Nevertheless, the agreement is excellent, which gave us confidence to delve into the details of the calculations and understand how the "single-atom" nature of the systems affects CO binding.

The d-band center, d-band center of mass, and d-band filling are well-known descriptors affecting the CO adsorption energy on transition metal surfaces (*1*, *36*, *40*). When the outermost d-shell is full, as for group 11 metals, CO binding is dominated by d→2π* back-donation. When the d-shell is partially empty, as for group 9 metals, 5σ→d donation plays a more important role and even dominates in the case of Ir (*41*). Placing a metal atom on a metal-oxide support leads to the formation of chemical bonds, which affects the symmetry of the d-states as well as the filling. On this basis, one would expect the CO adsorption energy to differ from site to site and metal to metal and that there might be parallels with metal-oxide surfaces.

To understand how the nature of the single-atom catalysis site affects the CO adsorption energy, an extensive set of calculations was performed in which CO adsorption on each $Me_1/Fe_3O_4(001)$ system was compared with CO (i) in an on-top site of the corresponding (111) metal surface and (ii) on surface cation sites at the most stable facets of the respective metal oxide. The full dataset, all acquired using the same computational setup, is shown and discussed in the supplementary materials. In what follows, we discuss three representative metals, Ni, Ag, and Ir, which allow us to illustrate the most important factors involved. We found that the reactivity of metals was governed by electronic structure but that CO-induced structural distortions modulate the CO adsorption energy, particularly when the coordination is low.

It would be reasonable to expect that the oxide-supported metal adatoms should have properties somewhat in between a pure metal and a metal oxide. This case was exemplified by the Ni adatom, which exhibited a Bader charge (+0.68*e*) midway between the metal surface (+0.01*e*) and a fivefold-coordinated cation at the NiO(100) surface (+1.19*e*). Because the cations in NiO are nominally 2+, we assigned a 1+ oxidation state for the $Ni_1/Fe_3O_4(001)$ adatom. Ni^{1+} is not common in

nature, which immediately shows that unusual properties can arise when metal atoms are stabilized in undercoordinated geometries. In Fig. 3A, we plot the CO adsorption energy [E_{ads}(CO)] as a function of d-band center of mass for the three different environments mentioned above. As the metal atom becomes more oxidized (Bader charge increased), the d-band center of mass moves further below the Fermi energy E_F, and the CO binding weakens. If the Ni atom replaces a fivefold-coordinated Fe at the Fe_3O_4(001) surface, as has been observed in experiment (*42*), the system resembles NiO (100) because the local environment is almost identical. In this configuration, the d-band center of mass is far away from E_F and d→2π* back-donation cannot occur effectively, so the CO–Ni bond is primarily electrostatic (*43*).

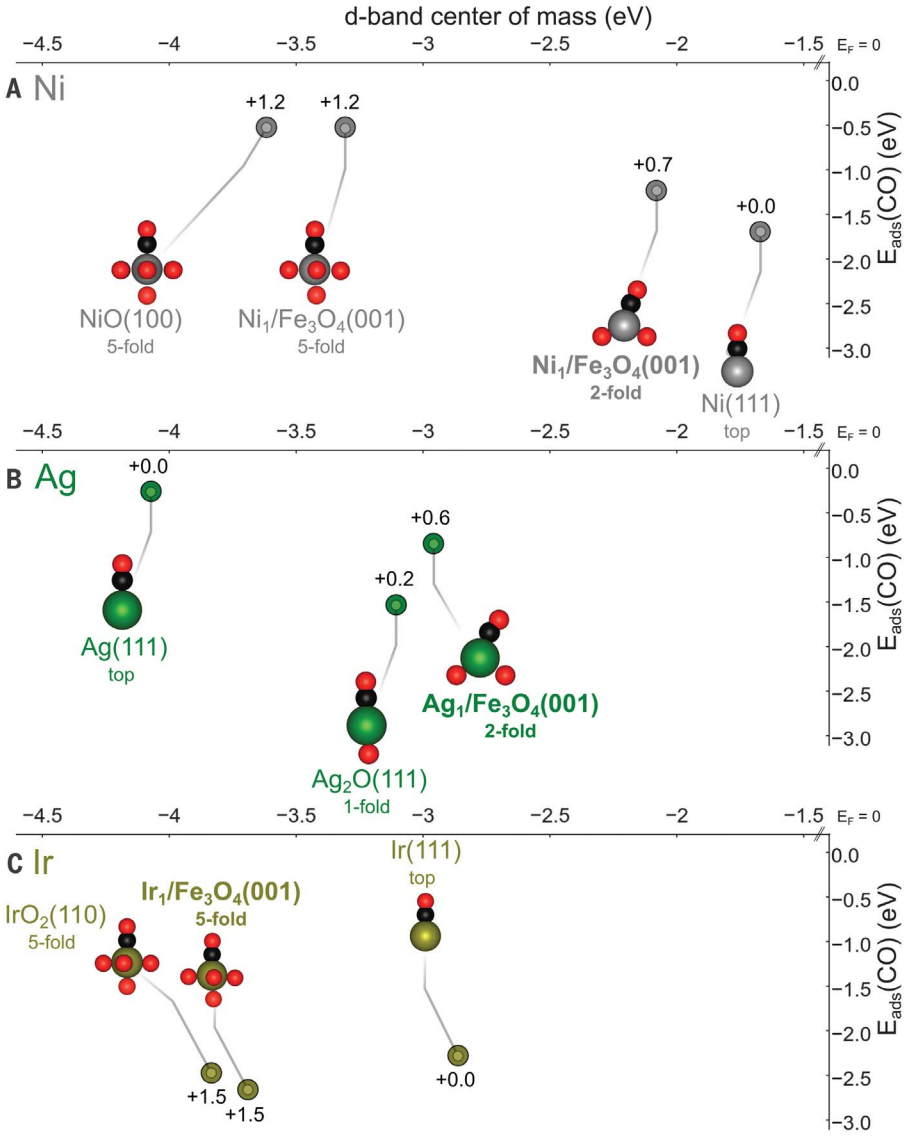

Fig. 3. CO adsorption energy for Me_1/Fe_3O_4(001) single-atom catalysts compared with Me(111) and MeO_x oxide surfaces, plotted against the d-band center of mass. The first coordination sphere of each configuration is illustrated with oxygen (red) and carbon (black), and each point is labeled with the corresponding Bader charge. (**A**) Nickel: As the oxidation state increases, the d-band center of mass moves away from E_F and the CO binding energy decreases. Ni incorporated into a fivefold site on Fe_3O_4(001) is close to NiO(100) because of the similar bonding environment. (**B**) Silver: Oxidized Ag has its d-band center of mass shifted toward E_F, leading to a stronger CO binding energy compared with the metal. The onefold-coordinated Ag atom on Ag_2O(111) exhibits a strong E_{ads}(CO) due to a linear $O_{surface}$–Ag–CO geometry. (**C**) Iridium: The E_{ads}(CO) at fivefold Ir_1/Fe_3O_4(001) is enhanced over Ir(111) because of the strong oxidation of the cation, which enhances 5σ→d donation. In this site, the Ir cation is similar to a cation in the IrO_2(110) surface.

In the case of Ag_1/Fe_3O_4(001) (Fig. 3B), CO is bound much more strongly than for the corresponding metal surface because the d-band center of mass shifts by 1.1 eV toward E_F in the twofold-coordinated adatom site. Because Ag retains a filled d-shell in the 1+ state, d→2π* back-donation continues to dominate, and the CO bond is substantially strengthened. However, the interaction is so strong that the Me_1-support bonds are weakened to accommodate the molecule in a more favorable geometry. Our reference calculations for the Ag_2O(111) surface suggest that the CO adsorption energy is optimal when the O–Me_1–CO bond angle is 180° (supplementary materials). Such an ideal geometry cannot be achieved at the Fe_3O_4(001) lattice, and the system comes to equilibrium when the energetic gain achieved by strengthening the Me_1–CO bond balances the cost of weakening the Me_1–O bonds. Thus, the adsorption energy is weaker than what would be expected on the basis of electronic structure of the adatom alone.

A similar distortion of the local structure was observed for all group 10 and 11 metals. In the Cu_1/Fe_3O_4(001) system, the adsorption energy was almost exactly the same as calculated for the metal surface. This situation is a coincidence, however, because the stronger bond caused by the upward shift in the d-band center of mass was almost exactly compensated by the large CO-induced distortion (Fig. 1, B and C). The most extreme consequence of CO-induced distortion is the sintering observed for Pd and Pt, where the formation of a stable carbonyl weakens the support interaction to such an extent that diffusion becomes facile even at room temperature.

Finally, Ir exhibited the strongest CO binding of all the systems considered in this work. Upon CO adsorption, the twofold-coordinated Ir adatom formed a bond to a subsurface O atom and created a pseudo–square-planar environment for the Ir atom (*29*). Binding a second CO molecule created a highly stable $Ir(CO)_2$ dicarbonyl with two bonds to surface oxygen (*29*), again highlighting the preference for the square-planar coordination. Dicarbonyls can be formed on almost all metals studied in this work, and the structure follows that expected on the basis of Me(I) coordination complexes (table S3 and associated discussion).

Regardless, the twofold Ir atom is ultimately unstable against incorporation into the Fe_3O_4(001) lattice and replaces a fivefold-coordinated Fe cation at ~450 K. Thus, CO desorption occurs from a fivefold Ir_1/Fe_3O_4(001) site in the temperature-programmed desorption experiment. Because the Ir–CO bonding is dominated by 5σ→d donation (*41*), the high oxidation state of the Ir atom (Bader charge = 1.5*e*) in this coordination enhances the CO adsorption energy. The downward shift in d-band center of mass weakens d→2π* back-donation,

but this is counteracted by the better alignment of the 5σ and d levels. Little distortion occurs when CO completes the favored sixfold-coordination environment (Fig. 2D), so the adsorption energy is purely based on the electronic structure. The fivefold $Ir_1/Fe_3O_4(001)$ site closely resembles a fivefold Ir cation at the rutile $IrO_2(110)$ surface in terms of Bader charge, location of the d-band center of mass, and E_{ads}(CO). This result suggests that fivefold Ir single-atom catalysts could be cost-effective replacements for IrO_2 electrocatalysts for water splitting, which are highly effective but prohibitively expensive.

Whether a metal incorporates into the Fe_3O_4 support is governed by the oxygen affinity and preferential O coordination. Table S7 lists the overall energetic gains moving from a two- to a fivefold site. The group 11 elements will not incorporate because they prefer the twofold coordination in their bulk oxide and would be oversaturated in a fivefold geometry. The group 10 elements Pd and Pt prefer to be fourfold coordinated to oxygen and have similar energies for two- and fivefold geometries studied in this work. In any case, neither is competitive against sintering into clusters, so incorporation does not occur. Last, the group 9 elements as well as Ni prefer incorporation into the lattice because they have a high oxygen affinity and have octahedral coordination in their most stable oxide.

The implications of our results for single-atom catalysis are twofold. The choice of metal for a specific reaction is generally governed by the Sabatier principle, which states that the optimum catalyst should be reactive enough to adsorb and activate reactants but not so reactive that the rate is hampered by sluggish desorption of products. Single-atom catalysis was originally developed because expensive metals such as Pt exhibit the optimal balance and sit at the top of a "volcano plot." Our study shows that binding the metal atoms to an oxide alters their electronic structure. For most metals, the twofold binding site strongly shifted the d-band center of mass toward E_F and increased the metal–CO bond strength. This resulted in shorter Me–C bond lengths compared with the metal surface (table S4). Moreover, because adsorption energies are a good proxy for activation barriers (*44*), we conclude that the metal adatoms become more reactive, so the metals previously limited by poor reactivity will shift closer to the top of a volcano plot. We refer to bond strength here, not adsorption energy, because the structural distortions render these two quantities inequivalent for the twofold-coordinated structures.

This result also has consequences for the catalysts limited by product desorption because destabilization by structural distortions will lead to product desorption at lower temperatures, that is, avoid poisoning by adsorbed products. Stabilizing low-coordination "single-atom" sites could provide ways to tailor the activity of specific metals and allow non–Pt-group metals to become competitive. This conclusion is in line with two recent theoretical screening studies (*14*, *16*) suggesting that FeO_x-supported Pd_1, Rh_1, Ru_1, and even Ti_1 or Co_1 species can have similar activity as Pt_1 for CO oxidation.

Knowledge of the local geometry is thus essential to understand the adsorption properties of supported metal adatoms. The observed properties stem directly from how the particular metal reacts to a particular bonding environment, and we observed a preference for the systems to adopt the coordination and bond angles seen in corresponding coordination complexes when CO is adsorbed. This, coupled to the observed ability of the single-atom catalysis systems to distort the structure to accommodate reactants, suggests that adsorbed single atoms should be viewed as undercoordinated complexes and not as the smallest possible nanoparticle. The results seen in this work will be transferrable to many oxide supports, including zeolites, which also offer a twofold-coordination environment. Particularly stable configurations are possible if the metal-oxide system forms solid solution in the bulk [e.g., the fivefold $Ni/Fe_3O_4(001)$], in which case the metal site is straightforward to predict. Although we observed a clear driving force for higher coordination (incorporation) for many of the metals studied in this work, low coordination to the oxide could be stabilized by the adsorption of additional ligands (reactants, OH, water) in the reactive environment, provided that these create a stable geometry for the metal atom. If control of the active site can be achieved in industrial systems, single-atom catalysts really do have the potential to combine the best of heterogeneous and homogeneous catalysis.

REFERENCES AND NOTES

1. B. Hammer, Y. Morikawa, J. K. Norskov, *Phys. Rev. Lett.* **76**, 2141–2144 (1996).
2. X. F. Yang *et al.*, *Acc. Chem. Res.* **46**, 1740–1748 (2013).
3. S. Liang, C. Hao, Y. Shi, *ChemCatChem* **7**, 2559–2567 (2015).
4. J. Liu, *ACS Catal.* **7**, 34–59 (2016).
5. B. C. Gates, M. Flytzani-Stephanopoulos, D. A. Dixon, A. Katz, *Catal. Sci. Technol.* **7**, 4259–4275 (2017).
6. A. Wang, J. Li, T. Zhang, *Nat. Rev. Chem.* **2**, 65–81 (2018).
7. H. Zhang, G. Liu, L. Shi, J. Ye, *Adv. Energy Mater.* **8**, 1701343 (2018).
8. K. Ding *et al.*, *Science* **350**, 189–192 (2015).
9. F. Chen, X. Jiang, L. Zhang, R. Lang, B. Qiao, *Chin. J. Catal.* **39**, 893–898 (2018).
10. X. Cui, W. Li, P. Ryabchuk, K. Junge, M. Beller, *Nat. Catal.* **1**, 385–397 (2018).
11. R. Lang *et al.*, *Angew. Chem. Int. Ed.* **55**, 16054–16058 (2016).
12. J. Liu, *Chin. J. Catal.* **38**, 1460–1472 (2017).
13. H. V. Thang, G. Pacchioni, L. DeRita, P. Christopher, *J. Catal.* **367**, 104–114 (2018).
14. J. Liang, Q. Yu, X. Yang, T. Zhang, J. Li, *Nano Res.* **11**, 1599–1611 (2018).
15. B. Qiao *et al.*, *Nat. Chem.* **3**, 634–641 (2011).
16. F. Li, Y. Li, X. C. Zeng, Z. Chen, *ACS Catal.* **5**, 544–552 (2014).
17. L. DeRita *et al.*, *Nat. Mater.* **18**, 746–751 (2019).
18. J. Resasco, S. Dai, G. Graham, X. Pan, P. Christopher, *J. Phys. Chem. C* **122**, 25143–25157 (2018).
19. R. Bliem *et al.*, *Science* **346**, 1215–1218 (2014).
20. G. S. Parkinson, *Surf. Sci. Rep.* **71**, 272–365 (2016).
21. Z. Novotný *et al.*, *Phys. Rev. Lett.* **108**, 216103 (2012).
22. B. Arndt *et al.*, *Surf. Sci.* **653**, 76–81 (2016).
23. G. S. Parkinson *et al.*, *Nat. Mater.* **12**, 724–728 (2013).
24. R. Bliem *et al.*, *ACS Nano* **8**, 7531–7537 (2014).
25. R. Bliem *et al.*, *Phys. Rev. B* **92**, 075440 (2015).
26. R. Bliem *et al.*, *Proc. Natl. Acad. Sci. U.S.A.* **113**, 8921–8926 (2016).
27. M. Meier *et al.*, *Nanoscale* **10**, 2226–2230 (2018).
28. P. T. P. Ryan *et al.*, *Phys. Chem. Chem. Phys.* **20**, 16469–16476 (2018).
29. Z. Jakub *et al.*, *Angew. Chem. Int. Ed.* **58**, 13961–13968 (2019).
30. Z. Jakub *et al.*, *Nanoscale* **12**, 5866–5875 (2020).
31. A. Walsh, A. A. Sokol, J. Buckeridge, D. O. Scanlon, C. R. A. Catlow, *Nat. Mater.* **17**, 958–964 (2018).
32. S. L. Hemmingson, C. T. Campbell, *ACS Nano* **11**, 1196–1203 (2017).
33. N. J. O'Connor, A. S. M. Jonayat, M. J. Janik, T. P. Senftle, *Nat. Catal.* **1**, 531–539 (2018).
34. J. Hulva *et al.*, *J. Phys. Chem. B* **122**, 721–729 (2018).
35. J. Hulva, T. U. Wien, thesis, TU Wien (2019).
36. M. Gajdoš, A. Eichler, J. Hafner, *J. Phys. Condens. Matter* **16**, 1141–1164 (2004).
37. P. A. Redhead, *Vacuum* **12**, 203–211 (1962).
38. C. T. Campbell, L. H. Sprowl, L. Árnadóttir, *J. Phys. Chem. C* **120**, 10283–10297 (2016).
39. M. J. Gillan, D. Alfè, A. Michaelides, *J. Chem. Phys.* **144**, 130901 (2016).
40. A. Stroppa, G. Kresse, *New J. Phys.* **10**, 063020 (2008).
41. M. T. M. Koper, R. A. van Santen, S. A. Wasileski, M. J. Weaver, *J. Chem. Phys.* **113**, 4392–4407 (2000).
42. Z. Jakub *et al.*, *J. Phys. Chem. C* **123**, 15038–15045 (2019).
43. G. Pacchioni *et al.*, *J. Phys. Condens. Matter* **16**, S2497–S2507 (2004).
44. L. C. Grabow, B. Hvolbæk, J. K. Nørskov, *Top. Catal.* **53**, 298–310 (2010).

ACKNOWLEDGMENTS

We thank P. Blaha (TU Wien) and P. T. P. Ryan (Imperial College London) for useful discussions. **Funding:** G.S.P., J.H., M.M., Z.J., and R.B. acknowledge funding from the Austrian Science Foundation (FWF) Start Prize (Y847-N20), and U.D. and F.K. acknowledge the Austrian Science Fund FWF (Project Wittgenstein Prize, Z250-N27). G.S.P. and M.M. acknowledge funding from the European Research Council (ERC) under the European Union's HORIZON2020 Research and Innovation program (ERC grant agreement 864628). Z.J. also acknowledges support from the TU Wien Doctoral College TU-D. The computational results were achieved in part by using the Vienna Scientific Cluster (VSC 3 and VSC 4). **Author contributions:** J.H. and R.B. performed the experiments under the supervision of G.S.P., who conceptualized the research and acquired research funding for the project. M.M. performed the theoretical calculations under the supervision of C.F. J.H., M.M., and G.S.P. wrote the paper with substantial input and revision from U.D., M.S., F.K., Z.J., and C.F. **Competing interests:** The authors declare no competing interests. **Data and materials availability:** All data are available in the main text or the supplementary materials.

SUPPLEMENTARY MATERIALS

science.sciencemag.org/content/371/6527/375/suppl/DC1
Materials and Methods
Supplementary Text
Figs. S1 to S14
Tables S1 to S7
References (*45*–*95*)

31 August 2020; accepted 9 December 2020
10.1126/science.abe5757

Science

Unraveling CO adsorption on model single-atom catalysts

Jan Hulva, Matthias Meier, Roland Bliem, Zdenek Jakub, Florian Kraushofer, Michael Schmid, Ulrike Diebold, Cesare Franchini and Gareth S. Parkinson

Science **371** (6527), 375-379.
DOI: 10.1126/science.abe5757

Modeling single-atom reactivity

Noble metals often perform best for demanding reactions such as oxygen reduction, an effect often explained by the position of their d-band. One way to minimize the cost of noble metals is to disperse them as single atoms. To model the reactivity of supported single atoms, Hulva *et al.* evaporated different transition metals such as nickel, silver, and iridium on an Fe_3O_4(001) support. Single atoms adsorbed in the same twofold site between underlying rows of surface iron atoms. In studies of CO adsorption as a proxy for reactivity, the d-band was strongly affected by the charge transfer to the support and CO-induced structural changes. These effects can weaken the adsorption energy compared with the expected values based on electronic structure alone.

Science, this issue p. 375